JACS
JOURNAL OF THE AMERICAN CHEMICAL SOCIETY
pubs.acs.org/JACS
Article

Sub-2 nm Ultrasmall High-Entropy Alloy Nanoparticles for Extremely Superior Electrocatalytic Hydrogen Evolution

Guang Feng,[⊥] Fanghua Ning,[⊥] Jin Song, Huaifang Shang, Kun Zhang, Zhengping Ding, Peng Gao, Wangsheng Chu,* and Dingguo Xia*

Cite This: J. Am. Chem. Soc. 2021, 143, 17117−17127
Read Online
ACCESS | Metrics & More | Article Recommendations | Supporting Information

ABSTRACT: The development of sufficiently effective catalysts with extremely superior performance for electrocatalytic hydrogen production still remains a formidable challenge, especially in acidic media. Here, we report ultrasmall high-entropy alloy (us-HEA) nanoparticles (NPs) with the best-level performance for hydrogen evolution reaction (HER). The us-HEA (NiCoFePtRh) NPs show an average diameter of 1.68 nm, which is the smallest size in the reported HEAs. The atomic structure, coordinational structure, and electronic structure of the us-HEAs were comprehensively clarified. The us-HEA/C achieves an ultrahigh mass activity of 28.3 A $mg^{-1}_{noble\ metals}$ at −0.05 V (vs the reversible hydrogen electrode, RHE) for HER in 0.5 M H_2SO_4 solution, which is 40.4 and 74.5 times higher than those of the commercial Pt/C and Rh/C catalysts, respectively. Moreover, the us-HEA/C demonstrates an ultrahigh turnover frequency of 30.1 s^{-1} at 50 mV overpotential (41.8 times higher than that of the Pt/C catalyst) and excellent stability with no decay after 10 000 cycles. Operando X-ray absorption spectroscopy and theoretical calculations reveal the actual active sites, tunable electronic structures, and a synergistic effect among five elements, which endow significantly enhanced HER activity. This work not only engineers a general and scalable strategy for synthesizing us-HEA NPs and elucidates the complex structural information and catalytic mechanisms of multielement HEA system in depth, but also highlights HEAs as sufficiently advanced catalysts and accelerates the research of HEAs in energy-related applications.

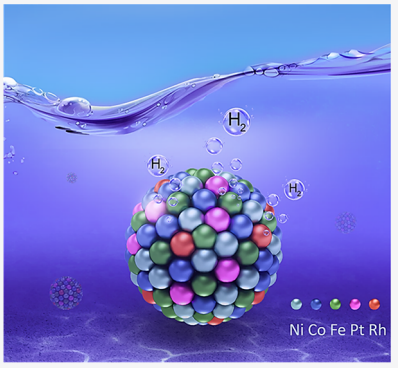

INTRODUCTION

Electrocatalytic water splitting is universally considered as an efficient and available technology to produce hydrogen fuel for renewable energy storage and carbon neutrality.[1,2] Hydrogen production can achieve an ultrahigh hydrogen purity of 99.995%, excellent energy efficiency, and fast kinetics process, especially in acidic media.[1,3] To date, numerous reports have explored advanced electrocatalysts for hydrogen evolution reaction (HER).[4−15] Even though these reported catalysts appear promising, they still cannot meet the necessary requirements for practical use in acidic media. Thus, major challenges still remain for research efforts focused on seeking other kinds of sufficiently advanced HER catalysts with extremely superior performance.

High-entropy alloys (HEAs) have demonstrated significant potential applications in many fields due to their unique and fascinating properties.[16−22] Moreover, HEAs have garnered increased attentions and become one of the hottest materials. Given their tunable composition, electronic structure, and significant stability in corrosive media, HEAs highly meet the necessary requirements of becoming advanced electrocatalysts. However, HEAs have only recently been researched in electrocatalysis,[23−27] and the characteristics and properties are preliminarily investigated and disclosed. Overall, the current HEA catalysts are suffering from various challenges. Especially, the current synthesis methods of HEAs are rather complex or not general strategies, the structural information on HEA catalysts has not been deeply revealed, the potential catalytic performance of HEAs have not been sufficiently explored, and the complicated catalytic mechanism of HEAs has not been clearly clarified. Therefore, a more rational design of HEAs is urgently needed to support HEAs as sufficiently advanced catalysts, accelerating the research of HEAs in electrocatalysis fields.

Herein, we employ a general and facile chemical coreduction method to fabricate a series of carbon-supported ultrasmall high-entropy alloy (us-HEA) nanoparticles (NPs). The us-HEA (NiCoFePtRh) NPs exhibit a uniform distribution on carbon supports and an average particle size of 1.68 nm, which is the smallest size in the reported HEAs. High-angle annular dark-field scanning transmission electron microscopy (HAADF-STEM) imaging and X-ray absorption fine structure (XAFS) measurements reveal the atomic structure, electronic

Received: July 22, 2021
Published: September 23, 2021

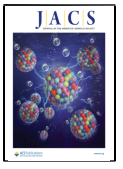

https://doi.org/10.1021/jacs.1c07643
J. Am. Chem. Soc. 2021, 143, 17117−17127

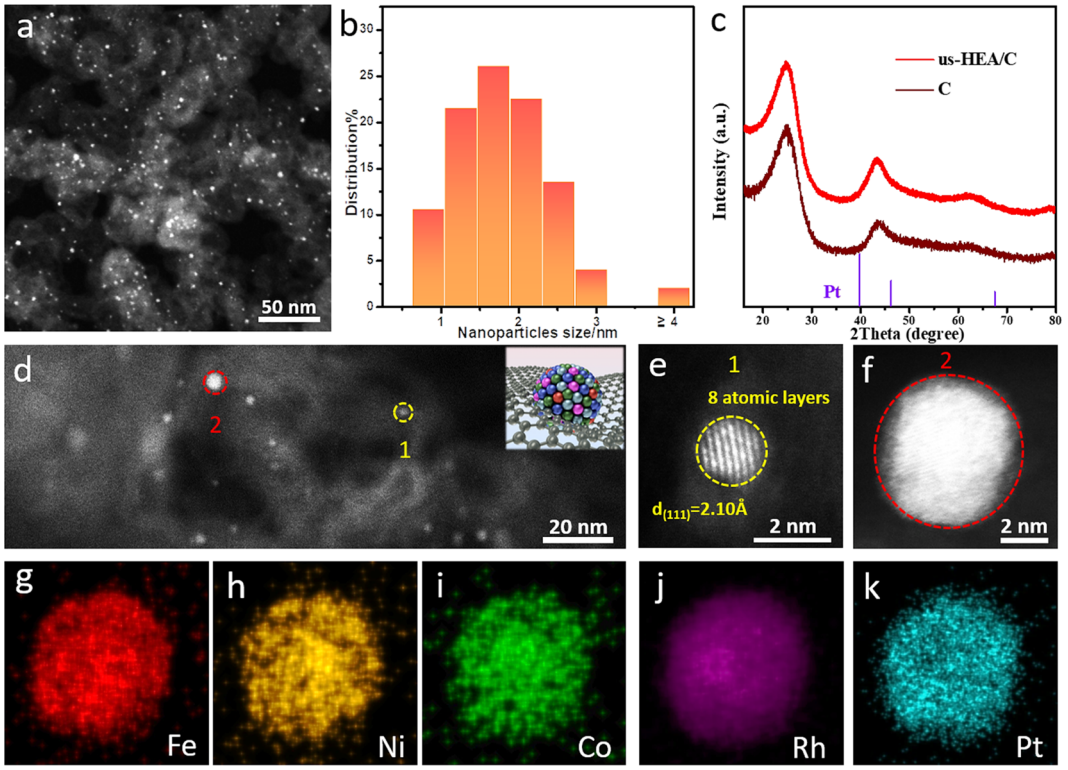

Figure 1. Morphology, structure, and composition characterization of ultrasmall NiCoFePtRh high-entropy alloy (us-HEA) nanoparticles (NPs). (a) Representative HAADF-STEM image and (b) size distribution histogram of us-HEA NPs. (c) X-ray diffraction (XRD) pattern of us-HEA/C. (d) Enlarged HAADF-STEM image (inset shows the model of NPs growing on the carbon support) of us-HEA/C NPs. (e) Lattice spacing of a single NP marked in (d), showing only eight atomic layers. (f) HAADF-STEM image of another single NP and the corresponding energy dispersive spectroscopy (EDS) elemental mapping of (g) Fe, (h) Ni, (i) Co, (j) Rh, and (k) Pt.

structure, and coordinational structure of us-HEAs. As an electrocatalyst for HER, us-HEA/C achieves an ultrahigh mass activity of 28.3 A $mg^{-1}_{noble\ metals}$ at −0.05 V (vs the reversible hydrogen electrode, RHE) in 0.5 M H_2SO_4 solution, which is 40.4 and 74.5 times higher than those of commercial Pt/C and Rh/C catalysts, respectively. Moreover, the us-HEA/C exhibits an ultrahigh turnover frequency (TOF) of 30.1 s^{-1} at 50 mV overpotential (41.8 times higher than that of the Pt/C catalyst) and excellent stability with no decay after 10 000 cycles. Operando X-ray absorption spectroscopy and theoretical calculations reveal the true active sites, tunable electronic structures, and a synergistic effect among five elements, which endow us-HEA/C with significantly enhanced HER activity. The outstanding performance of us-HEA NPs on HER provides a potential application as sufficiently advanced catalysts in practical electrocatalytic hydrogen production.

RESULTS AND DISCUSSION

Synthesis and Characterization of us-HEA NPs. Due to the vast difference in chemical and physical properties of mixing elements, the controllable synthesis of ultrafine HEA NPs without separate phases is quite difficult. In this work, a suitable and scalable synthetic strategy was achieved that ensures the simultaneous reduction of the mixed metal salts (see the Experimental section in the Supporting Information for details). After the coreduction of five metal precursors and further annealing, single-phase NiCoFePtRh HEAs were ultimately obtained. The powder X-ray diffraction (PXRD) patterns (Figure S1) and energy dispersive spectroscopy (EDS) mapping (Figure S2) of the products provide direct evidence of the successful preparation of NiCoFePtRh HEAs. The XRD patterns reveal that the NiCoFePtRh HEAs have a face-centered cubic (fcc) structure, similar to that of pure Pt. However, the sharp (111) peak at 43.2° implies a large crystal size, which was further verified by the HAADF-STEM image in Figure S2. In order to prepare ultrasmall NPs with uniform dispersion, the carbon supports were added to the reaction solution prior to the coreduction of metal salts[28] and a series of comparative samples with different loadings were obtained (Figures S3 and S4). Finally, 5 wt % loading in theory was determined to be the most appropriate in this work, labeled as us-HEA/C. Figure 1a and Figure S5 illustrate the representative HAADF-STEM and TEM overview images of the 5 wt % us-HEA NPs loaded on the carbon support. The us-HEA NPs are uniformly dispersed on the carbon supports with an average diameter of 1.68 nm (Figure 1b), which is much smaller than those of other reported HEAs (Table S1). The XRD pattern (Figure 1c) further confirms the ultrasmall crystal structure because no obvious diffraction peak is detected, which agrees with a previous study on an ultrasmall Pt nanocrystal.[29] The enlarged HAADF-STEM image (Figure 1d) implies a strong metal−support interaction. To verify this strong interaction, the heat treatment temperature was increased to 550 °C, conventionally causing particle coarsening; the particle size and diffraction peaks had no significant changes (Figure S6). Figure 1e shows the high-resolution HAADF-STEM image of an us-HEA NP with only eight atomic layers. The lattice spacing is 2.10 Å, which is corresponding to the (111) plane of XRD patterns (Figure S1 and Figure 4), suggesting that us-HEA NPs have (111)

https://doi.org/10.1021/jacs.1c07643
J. Am. Chem. Soc. 2021, 143, 17117−17127

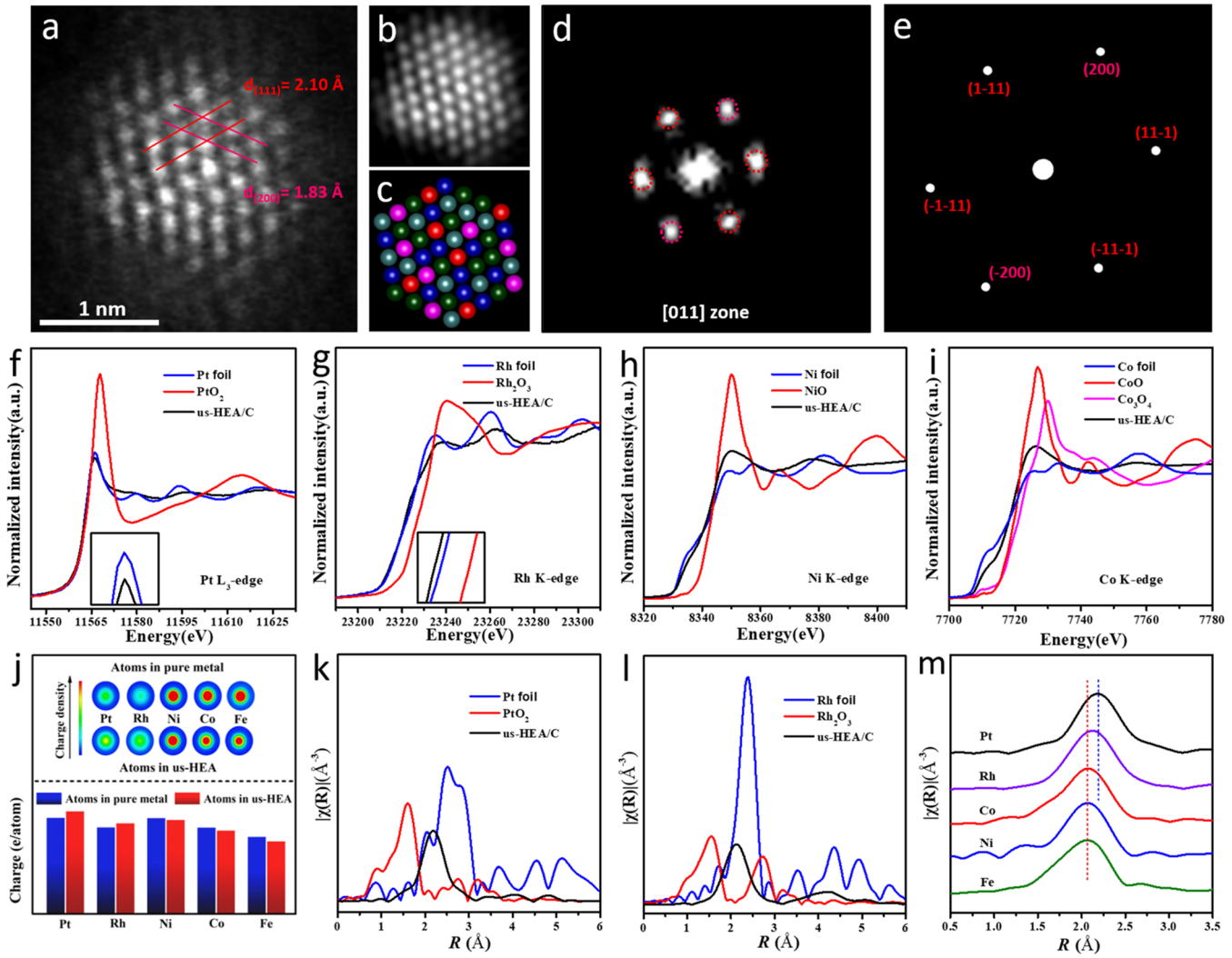

Figure 2. Characterization of atomic structure, electronic structure, and coordinational structure of us-HEA. (a) Atomically resolved HAADF-STEM image of an us-HEA NP. (b) Corresponding Fourier filtered image, (c) simulated crystal structure image, (d) fast Fourier transformation (FFT) pattern, and (e) simulated diffraction pattern from the [011] zone axis of a. (f) X-ray absorption near edge structure (XANES) spectra for the Pt L_3-edge. (g) XANES spectra for the Rh K-edge. (h) XANES spectra for the Ni K-edge. (i) XANES spectra for the Co K-edge. (j) Amount of electrons of the corresponding surface atom in pure metal and us-HEA (111) slab systems obtained from Bader charge analysis. The inset at the top is the two-dimensional charge density distributions of surface atoms in pure metals (Pt, Rh, Ni, Co, and Fe) and us-HEA (111) slab systems. The extended XAFS spectra for (k) Pt L_3-edge and (l) Rh k-edge. (m) Overlay of the extended XAFS spectra for all five X-ray probed elements in us-HEA/C.

basal planes and a fcc structure. EDS mapping and line scanning profiles of a single us-HEA NP are shown in Figure 1f–k and Figure S7a, respectively, revealing that all five elements are uniformly distributed and well-mixed without composition segregation. The atomic ratio of Ni/Co/Fe/Pt/Rh is 26.6:25.6:25.1:14.9:7.8 (Figure S7b), which is roughly in accordance with the overall composition analysis, measured by inductively coupled plasma-atomic emission spectroscopy (ICP-AES) (Table S2). It should be noted that long-time exposure under electron beams during the elemental mapping characterization would seriously damage the ultrasmall NP (Figure S8), so larger nanoparticles were selected to obtain clear elemental mapping.

The high-magnification aberration-corrected HAADF-STEM imaging technique was conducted to reveal the atomic structure of us-HEA. Figure 2a shows a characteristic atomic-resolution image of an us-HEA NP along the [011] zone axis, with lattice spacings of 2.10 and 1.83 Å attributed to the (111) and (200) planes, respectively. The corresponding Fourier filtered image and simulated crystal structure image (Figure 2b,c) illustrate that the us-HEA NP possesses an edge length of only 4–5 atoms. It is worth mentioning that this ultrasmall nanostructure can afford ultrahigh atom utilization, which further contributes to the ultrahigh utilization efficiency of noble metal atoms. The fast Fourier transformation (FFT) pattern is shown in Figure 2d, which matches well with the simulated diffraction patterns of an ideal us-HEA crystal along its [011] zone axis (Figure 2e).

XAFS measurements and computational simulation analyses were performed to further confirm the electronic structure of us-HEAs. Compared with the metal reference sample, the white line (WL) intensity of the Pt L_3-edge slightly decreased (Figure 2f) and the Rh K-edge slightly shifted to the left (Figure 2g), respectively, which indicates a transfer of the electron density from neighboring atoms to Pt and Rh atoms. The Fe, Co, and Ni K-edges in us-HEAs are all slightly shifted

https://doi.org/10.1021/jacs.1c07643
J. Am. Chem. Soc. 2021, 143, 17117–17127

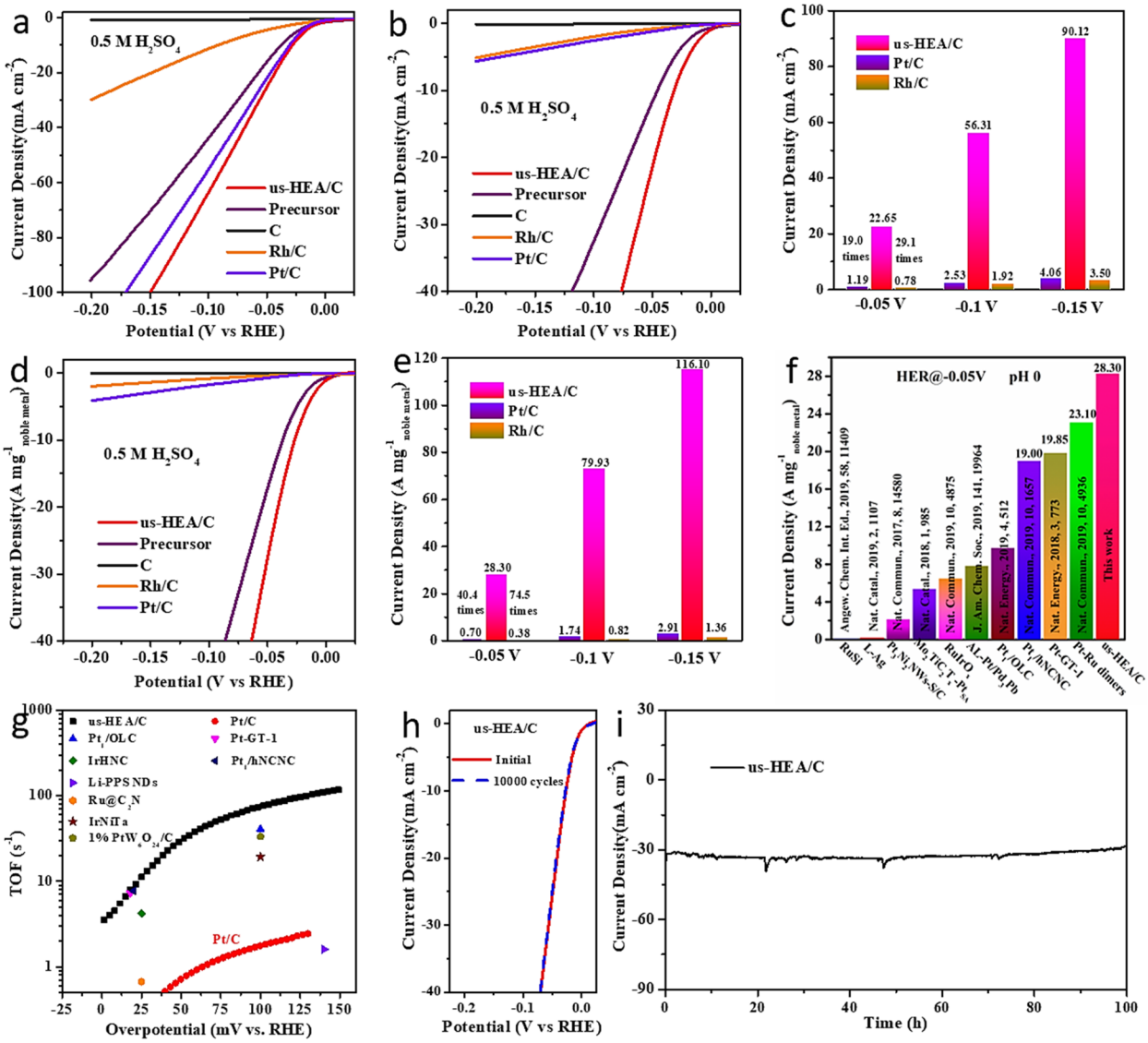

Figure 3. Electrocatalytic performance of us-HEA/C electrocatalyst for hydrogen evolution reaction (HER) in 0.5 M H_2SO_4 solution. (a) HER polarization curves of us-HEA/C, the precursor, C, commercial Rh/C, and commercial Pt/C, normalized by geometric area. (b) ECSA normalized HER polarization curves of us-HEA/C, the precursor, C, commercial Rh/C, and commercial Pt/C. (c) Quantitative comparisons of the specific activities normalized by ECSA of us-HEA/C, commercial Rh/C, and commercial Pt/C at different potentials. (d) Noble-metal mass loading normalized HER polarization curves of us-HEA/C, the precursor, C, commercial Rh/C, and commercial Pt/C. (e) Quantitative comparisons of the mass activities of us-HEA/C, commercial Rh/C, and commercial Pt/C at different potentials. (f) Mass activity comparisons of us-HEA/C at −0.05 V versus RHE with state-of-the-art noble metal catalysts reported in the recent literatures. (g) Turnover frequency (TOF) comparisons of us-HEA/C with other advanced noble metal catalysts reported previously. Stability tests of us-HEA/C through potential cycling 10 000 cycles, normalized by (h) geometric area and (i) constant applied potential for 100 h. All the results were not *iR* corrected.

to the right with respect to that of the metal reference sample (Figure 2h,i, and Figure S9), probably due to the low electronegativity of these three metals resulting in the donation of electron density. Here, it should be noted that the intensity variation of pre-edge and main features of these XANES at Fe, Co, and Ni K-edge is due to the intrinsic size effect of the ultrasmall NPs as pointed by Rehr,[30] rather than oxidation effect. The ab initio calculation simulated the XANES feature evolution with the size of the nanoparticle (Figures S10 and S11). All the white lines are far away from the corresponding oxide reference sample, indicating that all the elements in the us-HEA NPs are in metallic states. The result of Bader charge analysis also confirms the transfer of electron density in the us-HEA (Figure 2j). Overall, the above results indicate the redistribution of electrons and fine-tuning electronic structure of us-HEAs, while any change to the electronic structure will influence the electrocatalytic activity of the catalyst. As shown in Figure S12, the transfer of electron density from neighboring atoms to Pt atoms can effectively lower the Fermi level and the *d*-band center position of Pt.

The extended XAFS (EXAFS) spectra were used to further determine the entire coordination structure of five metallic elements in the us-HEAs. Figure S13 shows the experimental k^2-weighted EXAFS oscillations of us-HEA/C at Fe, Co, Ni, and Rh K-edge and Pt L_3-edge. The Fourier transforms (FT; No phase correction) of these EXAFS are displayed in Figure 2k,l and Figure S14, compared with the FT-EXAFS of the element metals and their oxides. The missing of the Me-O

https://doi.org/10.1021/jacs.1c07643
J. Am. Chem. Soc. 2021, 143, 17117−17127

(Me: Fe, Co, Ni, Rh, and Pt) shell (ca. 1.5 Å) for all FT curves of us-HEA/C means that the as-prepared sample is not oxidized. The distance of all the first shells (Me−Me) in us-HEAs is shorter than that of their element metals, respectively, especially for the FT of Rh and Pt. Figure 2m overlays all these FT curves for the first shell. The distance and amplitude are almost identical for the Fe, Co, and Ni absorbers, indicating that these 3d transition metals have an identical local atomic structure and completely random mixing distribution in us-HEAs. For Rh and Pt, the distance is a little longer because of their larger atomic radii. A quantitative local structure was obtained by fitting all the FT-EXAFS spectra. The quality of fits is shown in Figure S15, and the fitted structural parameters are summarized in Table S3. The fitting results show that the average coordination numbers (CNs) of the first shells are almost the same for all probed metals, around 8.5. This CN value means the size of us-HEAs is ca. 1.5 nm, according to the "growth curve" of CN as a function of nanoparticle size.[31] The interatomic distances (R) between Fe, Co, and Ni are identical, that is about 2.50 Å. The interatomic distance between Rh and Pt is about 3.85 Å. Hence, the EXAFS quantitative analysis suggests that these five metallic elements in us-HEAs form a solid-solution phase structure without elemental segregation.

Using the same synthesis method, eight other HEA NPs including PtRhAuIrPd, CoCuZnPtPd, NiCoCuPtAu, CdNiPtIrPd, CoNiCdPtPdIr, CoCdPtPdIrAu, CoNiCuCdPtPdIr, and FeCoNiCuCdPtIrPd HEA NPs, have also been synthesized. The representative elemental maps of quinary (PtRhAuIrPd, CoCuZnPtPd, NiCoCuPtAu, and CdNiPtIrPd), senary (CoNiCdPtPdIr and CoCdPtPdIrAu), septenary (CoNiCuCdPtPdIr), and octonary (FeCoNiCuCdPtIrPd) HEA NPs are shown in Figure S16. The elemental maps clearly reveal that each element in these HEAs is uniformly mixed without phase separation and provide direct evidence of alloy formation.[21] Therefore, our synthesis method was strongly demonstrated as a general strategy for the synthesis of high-entropy alloy NPs.

Electrochemical Performance of us-HEA NPs. The electrocatalytic HER activity of the us-HEA/C was investigated using a three-electrode setup in 0.5 M H_2SO_4 solution at room temperature. Several samples (including the commercial Pt/C, commercial Rh/C, Ketjen-black carbon (C), and precursors) were also measured under the same test conditions for comparison. In order to directly compare the performance with the reported catalysts under the same conditions, we investigated the activities of catalysts on the basis of the measured current densities in this work, which is consistent with previous works.[4,10,12,15,32] Figure 3a shows the specific activities normalized by geometric area without iR compensation. Considering that the HER is dominant in the polarization curves, the obtained current densities are mainly attributed to the HER, similar to other reported works.[4,12,13,25] It can be seen that, although the noble metal loading of the us-HEA/C is only 0.8224 μg cm^{-2}, much lower than that of commercial Pt/C (32 μg_{Pt} cm^{-2}) and other reported noble-metal catalysts (Table S4), the us-HEA/C exhibits a smaller overpotential (27 mV) at a current density of 10 mA cm^{-2}. The us-HEA/C exhibits a Tafel slope of 30.1 mV dec^{-1}, also lower than that of commercial Pt/C (30.5 mV dec^{-1}), demonstrating the Volmer−Tafel mechanism as the HER pathway (Figure S17). The Nyquist plots indicate that us-HEA/C has a fast kinetics for HER (Figure S18). To further characterize the activity of these catalysts, the specific activities shown in Figure 3b are all normalized to the electrochemically active surface area (ECSA) obtained by calculating the hydrogen absorption−desorption regions (Figure S19). As expected, the us-HEA/C exhibits the most favorable specific activities among these catalysts, with the highest current density in the entire potential region. At a potential of −0.05 V (vs RHE), the us-HEA/C exhibits an ultrahigh specific activity (22.65 mA cm^{-2}) (Figure 3c), which is 19.0 and 29.1 times higher than those of the commercial Pt/C (1.19 mA cm^{-2}) and Rh/C (0.78 mA cm^{-2}), respectively.

Meanwhile, the mass activity of us-HEA/C also confirms its ultrahigh activity for HER. Figure 3d presents the linear sweep voltammetry (LSV) curves of several catalysts normalized by noble metal mass, indicating that the us-HEA/C catalyst has an absolute advantage. The mass activity of us-HEA/C is high up to 28.3 A mg^{-1} at −0.05 V vs RHE (Figure 3e), which is 40.4 and 74.5 times greater than those obtained from commercial Pt/C (0.70 A mg^{-1}) and Rh/C (0.38 A mg^{-1}), respectively. Even compared with those of other advanced noble metal catalysts reported in the recent literatures (Figure 3f[4,12,13,32−40] and Tables S5 and S6), the mass activity (28.3 A mg^{-1}) of us-HEA/C can be proven as one of the best electrocatalysts for HER. These results suggest that the us-HEA can significantly increase the utilization of noble metals and decrease the cost of the catalyst. To obtain a deeper insight into the activities, the TOFs of the us-HEA/C and other reported catalysts are further investigated. As shown in Figure 3g[4,12,33,41−45] and Table S5, the us-HEA/C demonstrates higher TOFs than those of other noble-metal catalysts at various overpotentials. In particular, the TOF of 30.1 s^{-1} observed at 50 mV overpotential is 41.8 times higher than that of the Pt/C catalyst. The above results demonstrate that us-HEA/C has ultrahigh electrocatalytic activity for the HER, including outstanding specific activity, ultrahigh mass activity, and TOFs.

To evaluate the practicality of the catalyst, stability is another very important parameter, especially in acidic solutions. As shown in Figure 3h, as the accelerated degradation test (ADT) for 10 000 cycles between +0.1 and −0.2 V (vs RHE) at 100 mV s^{-1}, the polarization curve of the us-HEA/C catalyst does not exhibit any negative shift. In contrast, the polarization curves of both Pt/C and Rh/C have shown obvious deterioration after only 1000 cycles (Figure S20). Moreover, after the 10 000 cycles test, the morphology of the us-HEA remains intact with no obvious particle growth and agglomeration (Figure S21). As a sharp contrast, commercial Pt/C catalyst agglomerates severely. The XRD pattern (Figure S22), elemental distributions (Figure S23), and lattice fringes (Figure S24) of us-HEA/C after stability test exhibit no noticeable change, indicating that the high-entropy nanocrystals have excellent structural stability. The line scanning profile (Figure S25) of the us-HEA NPs collected after stability test evidence the superior compositional stability and corrosion resistance. Figure 3i shows a long-term stability test of the us-HEA/C for 100 h in the 0.5 M H_2SO_4 solution. After the harsh test for 85 h, us-HEA/C can maintain 100% of the initial current density (Figure S26). However, Pt/C and Rh/C only maintain 74.8% and 45.1% of the initial current densities, respectively (Figure S27). The above results fully demonstrate that the us-HEA NPs are remarkably stable. The excellent stability of the us-HEA/C can be attributed to the following reasons: first, the high-entropy stabilization effect and high metallic element diffusion barriers. Second, the annealed us-HEAs have good crystallinity, preventing elemental segregation and etching. Third, tight bonding between the us-HEA NPs

https://doi.org/10.1021/jacs.1c07643
J. Am. Chem. Soc. 2021, 143, 17117−17127

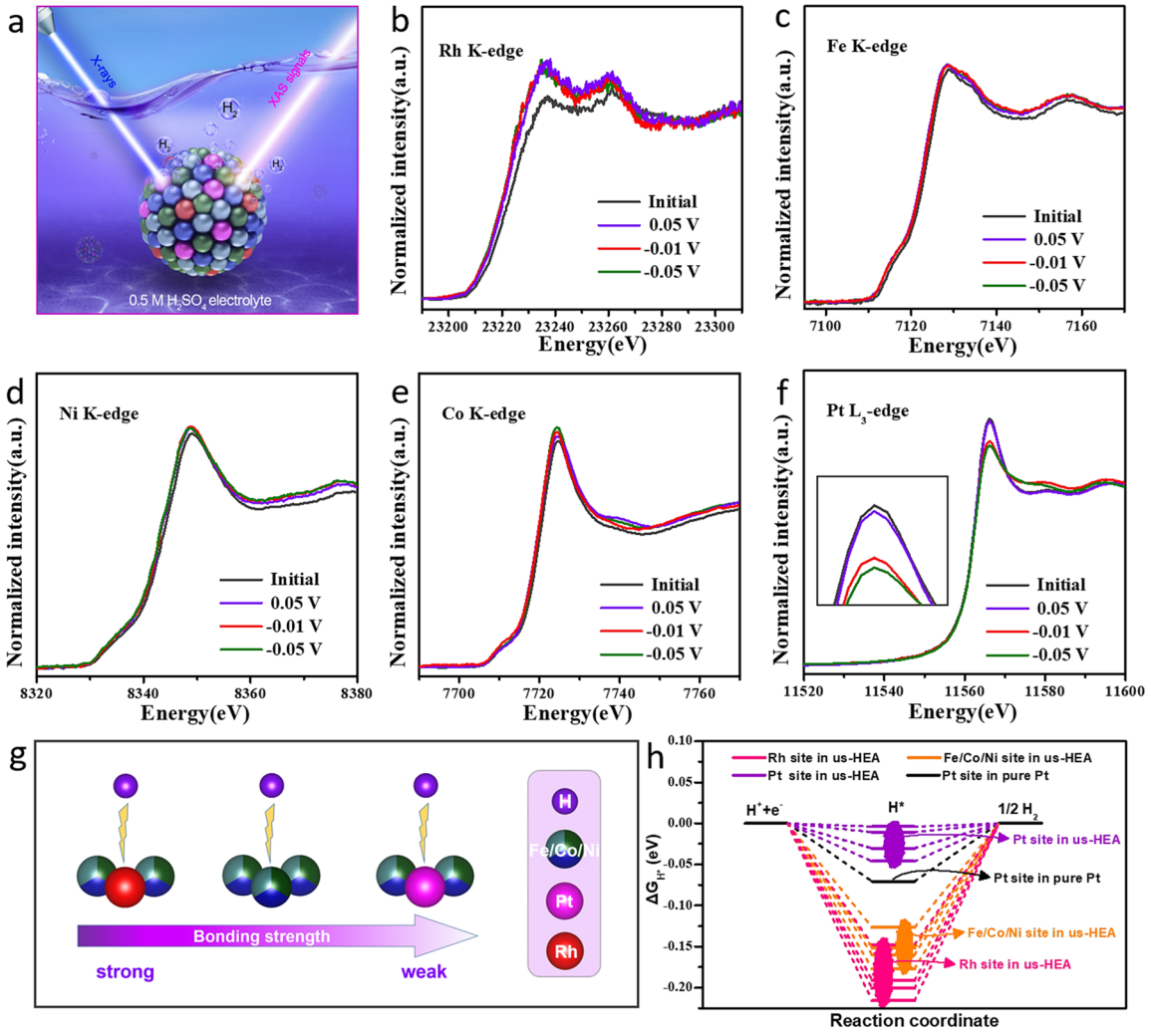

Figure 4. Operando X-ray absorption near-edge structure (XANES) measurements and theoretical calculations of hydrogen-adsorption free energies (ΔG_{H^*}). (a) Schematic illustration of the operando electrochemical test of the us-HEA catalyst during HER. In situ normalized XANES spectra of us-HEA/C recorded at different potentials in fluorescence mode at the (b) Rh K-edge, (c) Fe K-edge, (d) Ni K-edge, (e) Co K-edge, and (f) Pt L_3-edge (inset shows an enlarged view of the intensity). (g) Schematic illustration of the binding strength between H and the Rh site, Fe/Co/Ni site, and Pt site of us-HEA, respectively. (h) Calculated hydrogen-adsorption free energy (ΔG_{H^*}) profiles for three representative sites on the us-HEA (111) surface and Pt site on pure Pt (111) surface at monolayer hydrogen coverage (θ_{H^*} = 1).

and carbon substrate prevents NPs agglomeration or segregation during the tests. Fourth, the us-HEA NPs were synthesized in acidic solutions, so non-noble metal components, which are unstable or do not form alloys, were already etched out in the synthesis process.

In Situ X-ray Absorption near-Edge Structure (XANES) Analysis. The precise identification of the operando catalytic sites and elucidation of the practical reaction process under the electrochemical operation conditions is urgently required. However, the aforementioned remains challenging because of the structural complexity of catalysts and the difficulty of exploration, particularly for complex multielement systems (e.g., HEAs). Herein, we first employed in situ and operando X-ray absorption spectroscopy (XAS) to reveal the realistic reaction behaviors of HEAs, including the electronic state variation, identification of active sites, and parsing synergistic effect among the five elements. Figure 4a and Figure S28 show the schematic diagram of electrochemical operando XAS measurements and digital photograph of the operando fluorescence cell, respectively. Prior to XAS measurements, the sample was activated and each potential was held for ∼5 min to achieve a stable stage. The XANES spectra at Rh K-edge, Fe K-edge, Ni K-edge, Co K-edge, and Pt L_3-edge collected in fluorescence mode under the initial condition (immersed in H_2SO_4 solution) and different applied potentials are displayed in Figure 4b–f. The XANES for all applied voltages keeps their dominant features unchanged, especially for the positions of the WL and the second nearest oscillations. It means that the as-prepared HEA NPs stayed at a high stability in the reaction. When the cathodic potential of 0.05 V vs RHE (no HER occurs) was applied, the absorption edge of Rh dramatically shifted to a lower energy compared to the initial state, indicating that Rh gained numerous electrons and a large number of hydrogen ions were adsorbed on the surface of Rh sites. In contrast, the absorption edges of the other four elements changed a little. This is because hydrogen has a stronger adsorption binding strength at fcc sites with Rh nearby (Rh site) than those at fcc sites with only Fe/Co/Ni nearby (Fe/Co/Ni site) and at fcc sites with Pt nearby (Pt site) on the us-HEA (111) surface (Figure 4g). Hence,

https://doi.org/10.1021/jacs.1c07643
J. Am. Chem. Soc. 2021, 143, 17117−17127

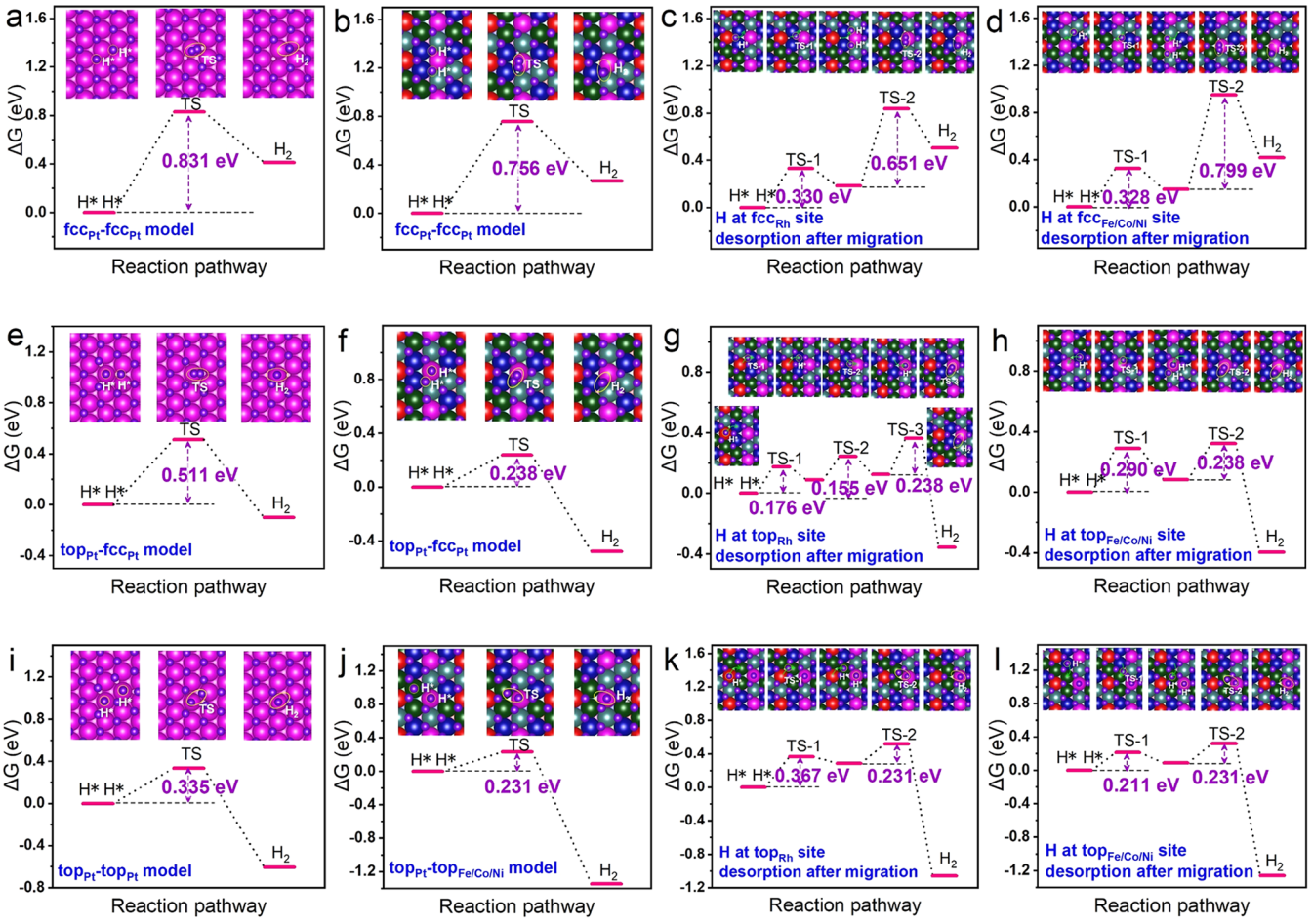

Figure 5. Tafel activation barriers from theoretical calculations. Free energy diagrams of the Tafel reaction on the basis of the (a–d) fcc–fcc, (e–h) top–fcc, and (i–l) top–top models on (a, e, and i) Pt (111) and (b–d, f–h, and j–l) us-HEA (111) surfaces. (a–d) Tafel reaction barrier on (a) Pt (111) surface for the fcc_{Pt}–fcc_{Pt} model and (b) us-HEA (111) surface for the fcc_{Pt}–fcc_{Pt} model and the desorption of H* at the (c) fcc_{Rh} and (d) $fcc_{Fe/Co/Ni}$ sites after migration. (e–h) Tafel reaction barrier on (e) Pt (111) surface for the top_{Pt}–fcc_{Pt} model and (f) us-HEA (111) surface for top_{Pt}–fcc_{Pt} model and the desorption of H* at (g) top_{Rh} and (h) $top_{Fe/Co/Ni}$ site after migration. (i–l) Tafel reaction barrier on (i) Pt (111) surface for the top_{Pt}–top_{Pt} model and (j) us-HEA (111) surface for the top_{Pt}–$top_{Fe/Co/Ni}$ model and desorption of H* at (k) top_{Rh} and (l) $top_{Fe/Co/Ni}$ site after migration. The inset shows the corresponding optimized adsorption structures for the initial state, the transition state (TS), and the final state.

hydrogen ions prefer to adsorb on Rh sites and the Rh site contributes greatly to the Volmer step in HER. The hydrogen adsorption on Rh site can also be confirmed by the intensity decrease of the peak at about 23260 eV versus the main peak (Figure S29 and Table S7).[46] With the increase in the applied potential to −0.01 and −0.05 V, the XANES spectra of Fe, Ni, and Co do not shift any further but also do not return to the original state (Figure S30), thus indicating that a small percentage of the Fe/Co/Ni sites participate in HER, while the Rh XANES edge continues to shift slightly to lower energy, suggesting that the number of hydrogen ions adsorbed on the surface of Rh sites increases and HER occurs directly on the Rh sites. Notably, the WL of the Pt XANES edge declines sharply when HER begins (−0.01 V), which amply illustrates that Pt sites are the main active sites for HER at this moment. The valence state of Rh and Pt with function of the edge position and the WL intensity, respectively, was plotted in Figure S31. The above operando XAS results show that both Rh and Pt are the main and direct active sites, which boost HER together.

Density Functional Theory (DFT) Calculations. Hydrogen-adsorption free energy (ΔG_{H^*}) is a widely used and reasonable descriptor for the ability of HER.[12,37,43] Figure 4h and Table S8 show the specifically calculated ΔG_{H^*} of HER for three types of representative sites (Figure S32) at monolayer hydrogen coverage ($\theta_{H^*} = 1$) on us-HEA (111) surface and Pt site on pure Pt (111) surface. The Pt site in the us-HEA has the smallest absolute ΔG_{H^*} (−0.004 eV) among the three types of representative sites on the us-HEA (111) surface and is smaller than that in pure Pt (−0.070 eV). The smaller absolute ΔG_{H^*} in us-HEA (111) surface was confirmed within three other structural models (Figures S33 and S34). The modified electronic structure of Pt in the us-HEA enables the Pt site to achieve an optimum Pt–H binding value, which might lead to a rapid H^+ adsorption and H_2 release process, ultimately accelerating HER.

But, only the ΔG_{H^*} descriptor cannot be representative for the HER activity. Peterson and co-workers have raised the concern on the challenge to the $\Delta G_{H^*} \sim 0$ interpretation of hydrogen evolution.[47] Therefore, to further reveal the origin of the superior activity and thoroughly elucidate the catalytic mechanism of us-HEA, we systematically studied the kinetic aspect in terms of the activation barrier of the rate limiting step, Tafel reaction. Three reaction models including fcc–fcc (desorption of two H* at fcc sites), top–fcc (desorption of one H* at top site and another H* at fcc site), and top–top

https://doi.org/10.1021/jacs.1c07643
J. Am. Chem. Soc. 2021, 143, 17117−17127

(desorption of two H* at top sites) models were investigated. On the basis of the fcc−fcc model at $\theta_{H^*} = 1$, the activation barrier for the Tafel step ($\Delta G_T^{\ddagger}$) on the Pt (111) surface is 0.831 eV (Figure 5a), which is consistent with that of 0.80−0.95 eV in Nørskov's work[48] and Peterson's work.[47] For the desorption of H* at the Pt site (fcc_{Pt} site) on the us-HEA (111) surface, the $\Delta G_T^{\ddagger}$ based on the fcc_{Pt}−fcc_{Pt} model is 0.756 eV (Figure 5b), which is considerably lower than that at the Pt (111) surface, indicating a faster desorption for two H* at the fcc_{Pt} site on the us-HEA (111) surface. The $\Delta G_T^{\ddagger}$ based on the fcc_{Rh}−fcc_{Rh} model is 0.884 eV (Figure S5a), which is higher than that of the fcc_{Pt}−fcc_{Pt} model. However, we identified two easier alternative desorption routes for H* at the fcc_{Rh} site. The first route is that the H* at the fcc_{Rh} site desorbs with the H* at the neighboring fcc_{Pt} site (fcc_{Rh}−fcc_{Pt} model), which shows a $\Delta G_T^{\ddagger}$ of 0.796 eV (Figure S35b), lower than that of the fcc_{Rh}−fcc_{Rh} model, even easier than that of the fcc−fcc model on the Pt (111) surface. The second route is that the H* at the fcc_{Rh} site migrates to the fcc_{Pt} site before desorption ($\theta_{H^*} = \frac{15}{16}$). The activation barrier for H* migration is as low as ∼0.33 eV, followed by a desorption of two H* at fcc_{Pt} sites with a relatively low activation barrier of 0.651 eV (Figure 5c). This indicates that the desorption of H* at the fcc_{Rh} site on the us-HEA (111) surface could be easier than that of H* at the fcc_{Pt} site on the Pt (111) surface. Similarly, we also analyzed the Tafel steps for H* at the $fcc_{Fe/Co/Ni}$ sites (Figure 5d and Figure S35c,d) and determined that they are similar to those H* at the fcc_{Rh} sites. The Tafel activation barriers of both the desorption of H* at $fcc_{Fe/Co/Ni}$ site with the H* at the neighboring fcc_{Pt} site ($fcc_{Fe/Co/Ni}$-fcc_{Pt} model) and the desorption of H* at $fcc_{Fe/Co/Ni}$ site assisted by H* migration from $fcc_{Fe/Co/Ni}$ to fcc_{Pt} site are lower than that on the Pt (111) surface. Hence, the desorption of H* at the fcc_{Pt}, fcc_{Rh}, and $fcc_{Fe/Co/Ni}$ sites on the us-HEA (111) surface could be all easier than that on the Pt (111) surface based on fcc-fcc model.

Furthermore, on the basis of the top−fcc model at $\theta_{H^*} = \frac{17}{16}$, $\Delta G_T^{\ddagger}$ on the Pt (111) surface is 0.511 eV (Figure 5e), which is consistent with previous works.[47,49] As for the us-HEA (111) surface, the activation barrier for the desorption of one H* at the Pt top site (top_{Pt} site) and another H* at the fcc_{Pt} site (top_{Pt}−fcc_{Pt} model) is only 0.238 eV (Figure 5f). The $\Delta G_T^{\ddagger}$ for the top_{Rh}−fcc_{Rh}model (Figure S36a) and desorption of H* at top_{Rh} after H* migration from top_{Rh} to top_{Pt} (Figure 5g) on the us-HEA (111) surface indicates that the desorption of H* at the top_{Rh} site could be easier than that of the top−fcc model on the Pt (111) surface. The desorption for H* at $top_{Fe/Co/Ni}$ sites on us-HEA (111) after H* migration from $top_{Fe/Co/Ni}$ to top_{Pt} site also show a lower $\Delta G_T^{\ddagger}$ than that on the Pt (111) surface on the basis of the top−fcc model (Figure 5h and Figure S36b). Thus, the Tafel reaction activity of H* at the top_{Pt}, top_{Rh}, and $top_{Fe/Co/Ni}$ sites on the us-HEA (111) surface could be superior to that on the Pt (111) surface on the basis of the top−fcc model. In addition, as shown in Figure 5i−l and Figure S37, the H* at the top_{Pt}, top_{Rh}, and $top_{Fe/Co/Ni}$ sites on the us-HEA (111) surface would show a faster desorption than that on the Pt (111) surface o nthe basis of the top−top model at $\theta_{H^*} = \frac{18}{16}$. In brief, $\Delta G_T^{\ddagger}$ values on the us-HEA (111) surface are lower than that on the Pt (111) surface, regardless of the fcc−fcc, top−fcc, and top−top models.

The calculations above reveal that the five elements in the us-HEA show a synergistic effect in Volmer−Tafel mechanism, enabled by the modified electronic structure. Pt sites on the us-HEA (111) surface show excellent activity in the Tafel step, while Rh and Fe/Co/Ni sites need the assistance of the Pt site in the Tafel step. The Rh element plays an important role in the Volmer step as the hydrogen adsorption energy is relatively low. Therefore, Pt and Rh elements are the main and direct active sites of us-HEA toward hydrogen evolution, verifying the operando XAS results. The Fe/Co/Ni atoms mainly play a role of effectively adjusting the electronic structures of Pt/Rh atoms and increasing the entropy of the us-HEAs to improve the stability.

On the basis of the discussion above, the origin of the ultrahigh hydrogen evolution activity of us-HEAs can be explained as follows. First, the us-HEA has ultrasmall nanoparticles and ultrahigh atom utilization. Second, there is a synergistic effect among the five atoms, which is also confirmed by experiments (Figure S37). Third, the us-HEA demonstrates tunable electronic structures, contributing to the optimum hydrogen-adsorption free energies and low activation barriers. All of the aforementioned characteristics contribute to the superior electrocatalytic activity of ultrasmall NiCoFePtRh HEA NPs toward hydrogen evolution.

CONCLUSION

In summary, we demonstrated the extremely superior performance and stability of novel NiCoFePtRh us-HEA NPs as an advanced and practical electrocatalyst in acidic media. The use of an ultrafast and powerful chemical coreduction method leads to the formation of uniform HEA nanocrystals with the smallest reported particle size (∼1.68 nm). HAADF-STEM and XAFS measurements reveal the atomic structure, electronic structure, and coordinational structure of us-HEAs. As an electrocatalyst for HER, us-HEA/C achieves an ultrahigh mass activity of 28.3 A $mg^{-1}_{noble\ metals}$ at −0.05 V, which is 40.4 and 74.5 times higher than those of the commercial Pt/C and Rh/C catalysts, respectively. Moreover, the us-HEA/C exhibits an ultrahigh TOF (30.1 s^{-1}) at a 50 mV overpotential (41.8 times higher than that of the Pt/C catalyst) and excellent stability with no decay after 10 000 cycles. Operando X-ray absorption spectroscopy and theoretical calculations reveal the actual active sites, fine-tuning of the electronic structure, and a synergistic effect among the five elements, which endow us-HEA with a significantly enhanced HER activity. The extraordinarily high performance of the supported us-HEA NPs provides a potential application as a sufficiently advanced HER catalyst for the storage of future renewable energy.

ASSOCIATED CONTENT

Supporting Information

The Supporting Information is available free of charge at https://pubs.acs.org/doi/10.1021/jacs.1c07643.

Discussions of experimental details, figures of PXRD patterns, HAADF-STEM images, EDS mappings, TEM images, line scanning profiles, EDS spectrum, XANES spectra, projected density of states, EXAFS oscillations, extended XAFS spectra, Tafel plots, Nyquist plots, CV curves, LSV curves, quantitative comparison of the current densities, stability tests, digital photograph of the operando fluorescence cell, diagram of corresponding adsorption sites, structural models, calculated hydrogen adsorption free energy profiles, free energy diagrams, and specific activities, and tables of HEAs reported

https://doi.org/10.1021/jacs.1c07643
J. Am. Chem. Soc. 2021, 143, 17117−17127

previously, ICP analysis, EXAFS fitting results, comparison of the geometric area activities of the advanced noble metal catalysts, comparison of the mass activities and TOFs of advanced noble metal catalysts, comparison of the commercial Pt/C catalysts, amplitude and position of the main two XANES features, and three types of representative sites (PDF)

AUTHOR INFORMATION

Corresponding Authors

Wangsheng Chu − *National Synchrotron Radiation Laboratory, University of Science and Technology of China, Hefei, Anhui 230029, P. R .China*; Email: chuws@ustc.edu.cn

Dingguo Xia − *Beijing Key Laboratory of Theory and Technology for Advanced Batteries Materials, College of Engineering and Beijing Innovation Center for Engineering Science and Advanced Technology, Peking University, Beijing 100871, P. R. China*; orcid.org/0000-0003-2191-236X; Email: dgxia@pku.edu.cn

Authors

Guang Feng − *Beijing Key Laboratory of Theory and Technology for Advanced Batteries Materials, College of Engineering, Peking University, Beijing 100871, P. R. China*

Fanghua Ning − *Beijing Key Laboratory of Theory and Technology for Advanced Batteries Materials, College of Engineering, Peking University, Beijing 100871, P. R. China*

Jin Song − *Beijing Key Laboratory of Theory and Technology for Advanced Batteries Materials, College of Engineering, Peking University, Beijing 100871, P. R. China*

Huaifang Shang − *Beijing Key Laboratory of Theory and Technology for Advanced Batteries Materials, College of Engineering, Peking University, Beijing 100871, P. R. China*

Kun Zhang − *Beijing Key Laboratory of Theory and Technology for Advanced Batteries Materials, College of Engineering, Peking University, Beijing 100871, P. R. China*

Zhengping Ding − *International Center for Quantum Materials & Electron Microscopy Laboratory, School of Physics, Peking University, Beijing 100871, P. R. China*; orcid.org/0000-0001-5275-5905

Peng Gao − *International Center for Quantum Materials & Electron Microscopy Laboratory, School of Physics, Peking University, Beijing 100871, P. R. China*; orcid.org/0000-0003-0860-5525

Complete contact information is available at: https://pubs.acs.org/10.1021/jacs.1c07643

Author Contributions

[⊥]G.F. and F.N. contributed equally to this work.

Notes

The authors declare no competing financial interest.

ACKNOWLEDGMENTS

This work was financially supported by the National Key R & D Program of China (No. 2016YFB0100200), the National Natural Science Foundation of China (No. 51671004 and U1764255), China Postdoctoral Science Foundation (2020T130004), and the Beijing Municipal Natural Science Foundation (No. 2181001). The first-principles calculations were supported by the High-Performance Computing Platform of Peking University. All support for our work is gratefully acknowledged.

REFERENCES

(1) Cabán-Acevedo, M.; Stone, M. L.; Schmidt, J. R.; Thomas, J. G.; Ding, Q.; Chang, H.-C.; Tsai, M.-L.; He, H.; Jin, S. Efficient hydrogen evolution catalysis using ternary pyrite-type cobalt phosphosulphide. *Nat. Mater.* **2015**, *14*, 1245−1251.

(2) Seh, Z. W.; Kibsgaard, J.; Dickens, C. F.; Chorkendorff, I.; Nørskov, J. K.; Jaramillo, T. F. Combining theory and experiment in electrocatalysis: Insights into materials design. *Science* **2017**, *355*, eaad4998.

(3) Esposito, D. V.; Levin, I.; Moffat, T. P.; Talin, A. A. H2 evolution at Si-based metal-insulator-semiconductor photoelectrodes enhanced by inversion channel charge collection and H spillover. *Nat. Mater.* **2013**, *12*, 562−568.

(4) Tiwari, J. N.; Sultan, S.; Myung, C. W.; Yoon, T.; Li, N.; Ha, M.; Harzandi, A. M.; Park, H. J.; Kim, D. Y.; Chandrasekaran, S. S.; Lee, W. G.; Vij, V.; Kang, H.; Shin, T. J.; Shin, H. S.; Lee, G.; Lee, Z.; Kim, K. S. Multicomponent electrocatalyst with ultralow Pt loading and high hydrogen evolution activity. *Nat. Energy* **2018**, *3*, 773−782.

(5) Yin, J.; Fan, Q.; Li, Y.; Cheng, F.; Zhou, P.; Xi, P.; Sun, S. Ni−C−N Nanosheets as Catalyst for Hydrogen Evolution Reaction. *J. Am. Chem. Soc.* **2016**, *138*, 14546−14549.

(6) Alinezhad, A.; Gloag, L.; Benedetti, T. M.; Cheong, S.; Webster, R. F.; Roelsgaard, M.; Iversen, B. B.; Schuhmann, W.; Gooding, J. J.; Tilley, R. D. Direct Growth of Highly Strained Pt Islands on Branched Ni Nanoparticles for Improved Hydrogen Evolution Reaction Activity. *J. Am. Chem. Soc.* **2019**, *141*, 16202−16207.

(7) Gu, G. H.; Lim, J.; Wan, C.; Cheng, T.; Pu, H.; Kim, S.; Noh, J.; Choi, C.; Kim, J.; Goddard, W. A.; Duan, X.; Jung, Y. Autobifunctional Mechanism of Jagged Pt Nanowires for Hydrogen Evolution Kinetics via End-to-End Simulation. *J. Am. Chem. Soc.* **2021**, *143*, 5355−5363.

(8) Zhu, E.; Yan, X.; Wang, S.; Xu, M.; Wang, C.; Liu, H.; Huang, J.; Xue, W.; Cai, J.; Heinz, H.; Li, Y.; Huang, Y. Peptide-Assisted 2-D Assembly toward Free-Floating Ultrathin Platinum Nanoplates as Effective Electrocatalysts. *Nano Lett.* **2019**, *19*, 3730−3736.

(9) Wang, Y.; Zhang, L.; Hu, C.; Yu, S.; Yang, P.; Cheng, D.; Zhao, Z.-J.; Gong, J. Fabrication of bilayer Pd-Pt nanocages with sub-nanometer thin shells for enhanced hydrogen evolution reaction. *Nano Res.* **2019**, *12*, 2268−2274.

(10) Kobayashi, D.; Kobayashi, H.; Wu, D.; Okazoe, S.; Kusada, K.; Yamamoto, T.; Toriyama, T.; Matsumura, S.; Kawaguchi, S.; Kubota, Y.; Aspera, S. M. e.; Nakanishi, H.; Arai, S.; Kitagawa, H. Significant Enhancement of Hydrogen Evolution Reaction Activity by Negatively Charged Pt through Light Doping of W. *J. Am. Chem. Soc.* **2020**, *142*, 17250−17254.

(11) Ali, A.; Shen, P. K. Recent Progress in Graphene-Based Nanostructured Electrocatalysts for Overall Water Splitting. *Electrochem. Energy Rev.* **2020**, *3*, 370−394.

(12) Liu, D.; Li, X.; Chen, S.; Yan, H.; Wang, C.; Wu, C.; Haleem, Y. A.; Duan, S.; Lu, J.; Ge, B.; Ajayan, P. M.; Luo, Y.; Jiang, J.; Song, L. Atomically dispersed platinum supported on curved carbon supports for efficient electrocatalytic hydrogen evolution. *Nat. Energy.* **2019**, *4*, 512−518.

(13) Zhang, J.; Zhao, Y.; Guo, X.; Chen, C.; Dong, C.-L.; Liu, R.-S.; Han, C.-P.; Li, Y.; Gogotsi, Y.; Wang, G. Single platinum atoms immobilized on an MXene as an efficient catalyst for the hydrogen evolution reaction. *Nat. Catal.* **2018**, *1*, 985−992.

(14) Kuang, Y.; Feng, G.; Li, P.; Bi, Y.; Li, Y.; Sun, X. Single-crystalline ultrathin nickel nanosheets array from in situ topotactic reduction for active and stable electrocatalysis. *Angew. Chem., Int. Ed.* **2016**, *55*, 693−697.

(15) Zheng, Y.; Jiao, Y.; Zhu, Y.; Li, L. H.; Han, Y.; Chen, Y.; Du, A.; Jaroniec, M.; Qiao, S. Z. Hydrogen evolution by a metal-free electrocatalyst. *Nat. Commun.* **2014**, *5*, 3783.

(16) Yao, Y.; Huang, Z.; Xie, P.; Lacey, S. D.; Jacob, R. J.; Xie, H.; Chen, F.; Nie, A.; Pu, T.; Rehwoldt, M.; Yu, D.; Zachariah, M. R.;

Wang, C.; Shahbazian-Yassar, R.; Li, J.; Hu, L. Carbothermal shock synthesis of high-entropy-alloy nanoparticles. *Science* **2018**, *359*, 1489−1494.
(17) Ding, Q.; Zhang, Y.; Chen, X.; Fu, X.; Chen, D.; Chen, S.; Gu, L.; Wei, F.; Bei, H.; Gao, Y.; Wen, M.; Li, J.; Zhang, Z.; Zhu, T.; Ritchie, R. O.; Yu, Q. Tuning element distribution, structure and properties by composition in high-entropy alloys. *Nature* **2019**, *574*, 223−227.
(18) Shi, P.; Ren, W.; Zheng, T.; Ren, Z.; Hou, X.; Peng, J.; Hu, P.; Gao, Y.; Zhong, Y.; Liaw, P. K. Enhanced strength-ductility synergy in ultrafine-grained eutectic high-entropy alloys by inheriting microstructural lamellae. *Nat. Commun.* **2019**, *10*, 489.
(19) McCormick, C. R.; Schaak, R. E. Simultaneous Multication Exchange Pathway to High-Entropy Metal Sulfide Nanoparticles. *J. Am. Chem. Soc.* **2021**, *143*, 1017−1023.
(20) Qiu, H.-J.; Fang, G.; Wen, Y.; Liu, P.; Xie, G.; Liu, X.; Sun, S. Nanoporous high-entropy alloys for highly stable and efficient catalysts. *J. Mater. Chem. A* **2019**, *7*, 6499−6506.
(21) Yao, Y.; Liu, Z.; Xie, P.; Huang, Z.; Li, T.; Morris, D.; Finfrock, Z.; Zhou, J.; Jiao, M.; Gao, J.; Mao, Y.; Miao, J.; Zhang, P.; Shahbazian-Yassar, R.; Wang, C.; Wang, G.; Hu, L. Computationally aided, entropy-driven synthesis of highly efficient and durable multielemental alloy catalysts. *Sci. Adv.* **2020**, *6*, eaaz0510.
(22) George, E. P.; Raabe, D.; Ritchie, R. O. High-entropy alloys. *Nat. Rev. Mater.* **2019**, *4*, 515−534.
(23) Xie, P.; Yao, Y.; Huang, Z.; Liu, Z.; Zhang, J.; Li, T.; Wang, G.; Shahbazian-Yassar, R.; Hu, L.; Wang, C. Highly efficient decomposition of ammonia using high-entropy alloy catalysts. *Nat. Commun.* **2019**, *10*, 4011.
(24) Wu, D.; Kusada, K.; Yamamoto, T.; Toriyama, T.; Matsumura, S.; Kawaguchi, S.; Kubota, Y.; Kitagawa, H. Platinum-Group-Metal High-Entropy-Alloy Nanoparticles. *J. Am. Chem. Soc.* **2020**, *142*, 13833−13838.
(25) Jia, Z.; Yang, T.; Sun, L.; Zhao, Y.; Li, W.; Luan, J.; Lyu, F.; Zhang, L. C.; Kruzic, J. J.; Kai, J. J.; Huang, J. C.; Lu, J.; Liu, C. T. A Novel Multinary Intermetallic as an Active Electrocatalyst for Hydrogen Evolution. *Adv. Mater.* **2020**, *32*, 2000385.
(26) Yao, Y.; Huang, Z.; Li, T.; Wang, H.; Liu, Y.; Stein, H. S.; Mao, Y.; Gao, J.; Jiao, M.; Dong, Q.; Dai, J.; Xie, P.; Xie, H.; Lacey, S. D.; Takeuchi, I.; Gregoire, J. M.; Jiang, R.; Wang, C.; Taylor, A. D.; Shahbazian-Yassar, R.; Hu, L. High-throughput, combinatorial synthesis of multimetallic nanoclusters. *Proc. Natl. Acad. Sci. U. S. A.* **2020**, *117*, 6316−6322.
(27) Huang, K.; Zhang, B.; Wu, J.; Zhang, T.; Peng, D.; Cao, X.; Zhang, Z.; Li, Z.; Huang, Y. Exploring the impact of atomic lattice deformation on oxygen evolution reactions based on a sub-5 nm pure face-centred cubic high-entropy alloy electrocatalyst. *J. Mater. Chem. A* **2020**, *8*, 11938−11947.
(28) Feng, G.; An, L.; Li, B.; Zuo, Y.; Song, J.; Ning, F.; Jiang, N.; Cheng, X.; Zhang, Y.; Xia, D. Atomically ordered non-precious Co3Ta intermetallic nanoparticles as high-performance catalysts for hydrazine electrooxidation. *Nat. Commun.* **2019**, *10*, 4514.
(29) Cheng, H.; Cao, Z.; Chen, Z.; Zhao, M.; Xie, M.; Lyu, Z.; Zhu, Z.; Chi, M.; Xia, Y. Catalytic System Based on Sub-2 nm Pt Particles and Its Extraordinary Activity and Durability for Oxygen Reduction. *Nano Lett.* **2019**, *19*, 4997−5002.
(30) Bazin, D.; Rehr, J. J. Limits and advantages of X-ray absorption near edge structure for nanometer scale metallic clusters. *J. Phys. Chem. B* **2003**, *107*, 12398−12402.
(31) Beale, A. M.; Weckhuysen, B. M. EXAFS as a tool to interrogate the size and shape of mono and bimetallic catalyst nanoparticles. *Phys. Chem. Chem. Phys.* **2010**, *12*, 5562−5574.
(32) Zhang, L.; Si, R.; Liu, H.; Chen, N.; Wang, Q.; Adair, K.; Wang, Z.; Chen, J.; Song, Z.; Li, J.; Banis, M. N.; Li, R.; Sham, T.-K.; Gu, M.; Liu, L.-M.; Botton, G. A.; Sun, X. Atomic layer deposited Pt-Ru dual-metal dimers and identifying their active sites for hydrogen evolution reaction. *Nat. Commun.* **2019**, *10*, 4936.
(33) Zhang, Z.; Chen, Y.; Zhou, L.; Chen, C.; Han, Z.; Zhang, B.; Wu, Q.; Yang, L.; Du, L.; Bu, Y.; Wang, P.; Wang, X.; Yang, H.; Hu, Z. The simplest construction of single-site catalysts by the synergism of micropore trapping and nitrogen anchoring. *Nat. Commun.* **2019**, *10*, 1657.
(34) Yao, Y.; Gu, X.-K.; He, D.; Li, Z.; Liu, W.; Xu, Q.; Yao, T.; Lin, Y.; Wang, H.-J.; Zhao, C.; Wang, X.; Yin, P.; Li, H.; Hong, X.; Wei, S.; Li, W.-X.; Li, Y.; Wu, Y. Engineering Electronic Structure of Submonolayer Pt on Intermetallic Pd3Pb via Charge Transfer Boosts Hydrogen Evolution Reaction. *J. Am. Chem. Soc.* **2019**, *141*, 19964−19968.
(35) Zhuang, Z.; Wang, Y.; Xu, C.-Q.; Liu, S.; Chen, C.; Peng, Q.; Zhuang, Z.; Xiao, H.; Pan, Y.; Lu, S.; Yu, R.; Cheong, W.-C.; Cao, X.; Wu, K.; Sun, K.; Wang, Y.; Wang, D.; Li, J.; Li, Y. Three-dimensional open nano-netcage electrocatalysts for efficient pH-universal overall water splitting. *Nat. Commun.* **2019**, *10*, 4875.
(36) Wang, P.; Zhang, X.; Zhang, J.; Wan, S.; Guo, S.; Lu, G.; Yao, J.; Huang, X. Precise tuning in platinum-nickel/nickel sulfide interface nanowires for synergistic hydrogen evolution catalysis. *Nat. Commun.* **2017**, *8*, 14580.
(37) Li, Z.; Fu, J.-Y.; Feng, Y.; Dong, C.-K.; Liu, H.; Du, X.-W. A silver catalyst activated by stacking faults for the hydrogen evolution reaction. *Nat. Catal.* **2019**, *2*, 1107−1114.
(38) Chen, H.; Ai, X.; Liu, W.; Xie, Z.; Feng, W.; Chen, W.; Zou, X. Promoting Subordinate, Efficient Ruthenium Sites with Interstitial Silicon for Pt-Like Electrocatalytic Activity. *Angew. Chem., Int. Ed.* **2019**, *58*, 11409−11413.
(39) Yan, Q.-Q.; Wu, D.-X.; Chu, S.-Q.; Chen, Z.-Q.; Lin, Y.; Chen, M.-X.; Zhang, J.; Wu, X.-J.; Liang, H.-W. Reversing the charge transfer between platinum and sulfur-doped carbon support for electrocatalytic hydrogen evolution. *Nat. Commun.* **2019**, *10*, 4977.
(40) Fang, S.; Zhu, X.; Liu, X.; Gu, J.; Liu, W.; Wang, D.; Zhang, W.; Lin, Y.; Lu, J.; Wei, S.; Li, Y.; Yao, T. Uncovering near-free platinum single-atom dynamics during electrochemical hydrogen evolution reaction. *Nat. Commun.* **2020**, *11*, 1029.
(41) Yu, F.-Y.; Lang, Z.-L.; Yin, L.-Y.; Feng, K.; Xia, Y.-J.; Tan, H.-Q.; Zhu, H.-T.; Zhong, J.; Kang, Z.-H.; Li, Y.-G. Pt-O bond as an active site superior to Pt^0 in hydrogen evolution reaction. *Nat. Commun.* **2020**, *11*, 490.
(42) Li, F.; Han, G.-F.; Noh, H.-J.; Jeon, J.-P.; Ahmad, I.; Chen, S.; Yang, C.; Bu, Y.; Fu, Z.; Lu, Y.; Baek, J.-B. Balancing hydrogen adsorption/desorption by orbital modulation for efficient hydrogen evolution catalysis. *Nat. Commun.* **2019**, *10*, 4060.
(43) Zhang, X.; Luo, Z.; Yu, P.; Cai, Y.; Du, Y.; Wu, D.; Gao, S.; Tan, C.; Li, Z.; Ren, M.; Osipowicz, T.; Chen, S.; Jiang, Z.; Li, J.; Huang, Y.; Yang, J.; Chen, Y.; Ang, C. Y.; Zhao, Y.; Wang, P.; Song, L.; Wu, X.; Liu, Z.; Borgna, A.; Zhang, H. Lithiation-induced amorphization of Pd3P2S8 for highly efficient hydrogen evolution. *Nat. Catal.* **2018**, *1*, 460−468.
(44) Mahmood, J.; Li, F.; Jung, S.-M.; Okyay, M. S.; Ahmad, I.; Kim, S.-J.; Park, N.; Jeong, H. Y.; Baek, J.-B. An efficient and pH-universal ruthenium-based catalyst for the hydrogen evolution reaction. *Nat. Nanotechnol.* **2017**, *12*, 441−446.
(45) Wang, Z. J.; Li, M. X.; Yu, J. H.; Ge, X. B.; Liu, Y. H.; Wang, W. H. Low-Iridium-Content IrNiTa Metallic Glass Films as Intrinsically Active Catalysts for Hydrogen Evolution Reaction. *Adv. Mater.* **2020**, *32*, 1906384.
(46) Morfin, F.; Blondeau, L.; Provost, K.; Malouche, A.; Piccolo, L.; Zlotea, C. Absorbed hydrogen enhances the catalytic hydrogenation activity of Rh-based nanocatalysts. *Catal. Sci. Technol.* **2018**, *8*, 2707−2715.
(47) Lindgren, P.; Kastlunger, G.; Peterson, A. A. A Challenge to the G∼ 0 Interpretation of Hydrogen Evolution. *ACS Catal.* **2020**, *10*, 121−128.
(48) Skúlason, E.; Tripkovic, V.; Björketun, M. E.; Gudmundsdóttir, S. d.; Karlberg, G.; Rossmeisl, J.; Bligaard, T.; Jónsson, H.; Nørskov, J. K. Modeling the electrochemical hydrogen oxidation and evolution reactions on the basis of density functional theory calculations. *J. Phys. Chem. C* **2010**, *114*, 18182−18197.
(49) Skúlason, E.; Karlberg, G. S.; Rossmeisl, J.; Bligaard, T.; Greeley, J.; Jónsson, H.; Nørskov, J. K. Density functional theory

calculations for the hydrogen evolution reaction in an electrochemical double layer on the Pt (111) electrode. *Phys. Chem. Chem. Phys.* **2007**, *9*, 3241−3250.

https://doi.org/10.1021/jacs.1c07643
J. Am. Chem. Soc. 2021, 143, 17117−17127